Completion of a Truncated Attenuation Image from the Attenuated PET Emission Data

Johan Nuyts[1], Christian Michel[2], Matthias Fenchel[3], Girish Bal[2], Charles Watson[2]

***Abstract*— Positron emission tomographs (PET) are currently almost exclusively designed as hybrid systems. The current standard is the PET/CT combination, while prototype PET/MRI systems are being studied by several research groups. One problem in these systems is that the transaxial field of view of the second system is smaller than that of the PET camera. The problem is limited for PET/CT, it is more pronounced in PET/MRI. Because this second system provides the image for attenuation correction, the smaller field of view causes truncation of the attenuation map. In this paper, we propose a maximum-a-posteriori algorithm for estimating the missing part of the attenuation map from the PET emission data.**

I. Introduction

In hybrid PET systems, there are two hurdles complicating the estimation of the PET attenuation map. One is the truncation mentioned already in the abstract, the other one is the conversion of the image values to linear attenuation coefficient at 511 keV. Although not fully solved for PET/CT systems, the current conversion methods produce satisfactory results in most cases. The problem is more difficult in MRI, because the MRI signal does not correlate with electron density. In this paper, this problem is not considered; we simply assume that an effective method is available for transforming the possibly truncated MRI image into the corresponding truncated PET attenuation image. An overview of existing methods is given in [1].

The problem of estimating the missing part of the attenuation map, is a milder version of the problem of simultaneously estimating the entire attenuation map (and the tracer distribution) from the attenuated emission data. The latter problem has been studied by several groups, both for PET and SPECT [2]–[9]. These algorithms can be roughly divided in three classes: algorithms based on 1) analytical consistency conditions, 2) discrete consistency conditions and 3) iterative reconstruction, often using the maximum likelihood criterion. Here, we present results on an adaptation of the iterative "MLAA" reconstruction algorithm of [5] to the problem at hand (MLAA stands for maximum likelihood reconstruction of attenuation and activity).

Recently, Salomon et al. proposed a related ML-algorithm, not for estimating the truncated region but for assigning attenuation values to MRI-regions, based on time-of-flight PET data [10], [11]. This algorithm is related to that of Laymon and Bowsher [12], who used a maximum likelihood approach to recover localized defects in the PET attenuation map.

In the following, the proposed (modified) MLAA algorithm is described. It has been evaluated on five PET/CT patient data sets, where the (nearly) untruncated CT-image was truncated to a reduced field-of-view. The truncated part of the CT-based attenuation map was estimated with MLAA, and the results were compared to those obtained with the original, untruncated attenuation map. We also examined the sensitivity of the MLAA-approach to segmentation errors in the known part of the attenuation map, and to scatter correction. Finally, a simulation experiment was done to assess the performance of the MLAA algorithm for reconstructing cold objects, such as coils, which are not included in the measured, truncated attenuation map.

[1] Nuclear Medicine, K.U.Leuven, B-3000 Leuven, Belgium, [2] Siemens Medical Solutions, MI, Knoxville, TN, USA, [3] Siemens AG, Erlangen, Germany

II. Methods

A. Objective function

Let $y_i, i = 1 \dots I$ represent the measured (attenuated) PET data acquired by detector pair i. The expectation $\bar{y}_i$ of the data y_i can be written as

$$\bar{y}_i = \sum_j g_{ij} a_i \lambda_j + s_i \quad \text{and} \quad a_i = \exp(-\sum_j l_{ij}\mu_j) \qquad (1)$$

where λ_j is the amount of radioactivity in j, g_{ij} is the probability that a unit activity in j contributes a detection event to line of response (LOR) i in absence of attenuation, a_i is the probability that a photon pair travelling along LOR i will not be attenuated, l_{ij} is the intersection length of LOR i with voxel j, μ_j is the linear attenuation coefficient in voxel j and s_i is an estimate of the scatter contribution.

Assuming perfect conversion from MRI values to linear attenuation coefficients, the MRI image provides reliable estimates of μ_j in the central part of the PET field of view. Outside that region, however, μ_j is unknown. Denoting the region where μ is known as K and its complement as U, we can write

$$a_i = m_i \exp(-\sum_{j\in U} l_{ij}\mu_j) \text{ with } m_i = \exp(-\sum_{j\in K} l_{ij}\mu_j) \qquad (2)$$

The PET data is acquired to produce the image $\hat{\lambda}$, which is an estimate of the true tracer distribution λ. To reconstruct this image from the data y, we have to estimate the unknown attenuation values $\{\mu_j, j \in U\}$ as well. Because PET data are Poisson distributed, the log-likelihood of this estimation problem can be written as

$$L(\hat{\lambda}, \hat{\mu}; y, m) = \sum_i y_i \ln(\hat{y}_i) - \hat{y}_i \qquad (3)$$

$$\hat{y}_i = \sum_j g_{ij} \hat{a}_i \hat{\lambda}_j + s_i \qquad (4)$$

$$\hat{a}_i = m_i \exp(-\sum_{j\in U} l_{ij}\hat{\mu}_j) \qquad (5)$$

This function is maximised to estimate $\hat{\mu}$ and $\hat{\lambda}$. Because this problem is under-determined, regularisation is recommended. To encourage smooth solutions of $\hat{\mu}$, two priors are combined for the attenuation image. The first prior $P_1(\hat{\mu})$ favours the attenuation coefficients of air and tissue. It is assumed that the truncated part will contain mostly air, tissue and bone, the lungs should be in the region K. The prior is created by combining Gaussian functions centered at the favoured

attenuation values [5]. This prior has obviously local maxima, and more so when the number of favoured attenuation values increases. For that reason, no additional mode for bone was added. The second prior $P_2(\hat{\mu})$ is the relative difference prior of [13]. This Markov prior is similar to the quadratic prior, except that it penalises relative differences between neighbouring pixels rather than absolute differences. In addition, it has a parameter (called γ in [13]) which optionally introduces increased tolerance of the prior to large relative differences.

The reconstruction of the activity image is also regularised with the relative difference prior. Because its parameters may be different from the parameters used in $P_2(\hat{\mu})$, we denote it with a different symbol $P_3(\hat{\lambda})$. Thus, the objective function L of (3) is replaced with the posterior function Q:

$$Q(\hat{\lambda}, \hat{\mu}; y, m) = L(\hat{\lambda}, \hat{\mu}; y, m) + P_1(\hat{\mu}) + P_2(\hat{\mu}) + P_3(\hat{\lambda}). \quad (6)$$

B. Optimisation

The reconstruction of the activity $\hat{\lambda}$ and of the missing attenuation $\hat{\mu}$ is obtained by maximising Q. As in [5], this is done by alternated maximisation. First, Q is increased by updating $\hat{\lambda}$, keeping $\hat{\mu}$ at its current value. Then, Q is further increased by updating $\hat{\mu}$. This sequence is considered a single iteration, and it is repeated until convergence is deemed satisfactory.

With fixed $\hat{\mu}$, the optimisation of Q reduces to standard maximum-a-posteriori (MAP) reconstruction in emission tomography. Hence, an update of $\hat{\lambda}$ is computed with a single iteration of a MAP-algorithm, here we used the algorithm proposed in [13]. In this step, the priors P_1 and P_2 can be ignored because they are independent of λ.

Combining (4) and (5) one obtains:

$$\hat{y}_i = (\sum_j g_{ij} \hat{\lambda}_j m_i) \exp(-\sum_{j \in U} l_{ij} \hat{\mu}_j). \quad (7)$$

Consequently, with fixed $\hat{\lambda}$, the optimisation of Q reduces to standard MAP reconstruction in transmission tomography. The first factor in (7) represents all the activity along LOR i, weighted with the detection probabilities g_{ij} and attenuated by the known attenuation in K. This quantity plays the role of the blank scan in standard transmission tomography. For the update of $\hat{\mu}$, we used a MAP reconstruction for transmission tomography [14] with the priors P_1 and P_2. The reconstruction was accelerated by using ordered subsets [15]. We used 6 iterations with 42 subsets.

C. Parameter values

The parameter γ was set to 5 in $P_1(\hat{\mu})$ and $P_2(\hat{\mu})$ and to 20 in $P_3(\hat{\lambda})$ based on visual inspection of the resulting images. We found that the results are not sensitive to the weight for the prior $P_3(\hat{\lambda})$. In contrast, the weights for the priors $P_1(\hat{\mu})$ and $P_2(\hat{\mu})$ had to be carefully tuned to obtain good results. However, the same set of parameters produced good results in all patients, suggesting that the method can be applied in clinical practice.

III. Results

A. Truncated CT-based attenuation maps

The method was evaluated in 5 ^{18}F-FDG whole body patient data sets from our PET/CT systems. The CT data were truncated to a central field of view of 40 cm, and the algorithm was applied to estimate the missing attenuation values. It was assumed that the shape, position and attenuation of the patient bed was known, and therefore, the patient bed was also inserted as a known portion into the truncated image.

The MLAA algorithm estimates both the attenuation and the activity, but the features of the activity image are different from the typical clinical images, because of the high number of iterations and the use of $P_3(\hat{\lambda})$. Therefore, a final "clinical" activity image is computed with OSEM using the MLAA-estimated attenuation map.

Emission images were reconstructed using 1) the untruncated attenuation map (reference), 2) the truncated attenuation map and 3) the truncated and completed attenuation map. These images were compared to assess the severity of truncation induced errors, and the performance of the proposed completion algorithm. The three final emission images were reconstructed with 3 OSEM iterations, using 21, 16 and 8 subsets respectively. Figure 1 shows maximum intensity projections of the three image sets (and their difference with the reference) for one particular patient. Figure 2 gives the relative errors in the reconstructed PET as a function of the reference standardised uptake value (SUV). Figure 3 shows the original, the truncated and MLAA-completed attenuation maps for the other 4 patient studies.

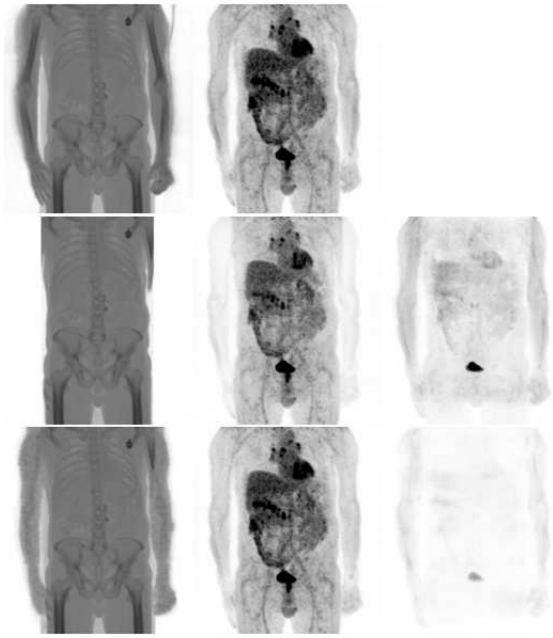

Fig. 1. The first row shows maximum intensity projections of the CT-based attenuation and the PET activity images. The second row shows the corresponding images in the case of truncation. The difference image reveals that activity values in the entire 3D PET image are affected. The third row shows the completed attenuation image and the corresponding PET image.

The truncation of the arms causes the SUV to be underestimated by 10 to 25%. After MAP-based estimation of the missing attenuation values, this error was reduced to about 5% in 4 studies. In the first study of figure 3 the error was larger (about 10%), but we suspect this is due to the truncation error in the original CT-image, which led to over-estimation of the attenuation in the arms (see figure 3), and therefore errors in the reference image.

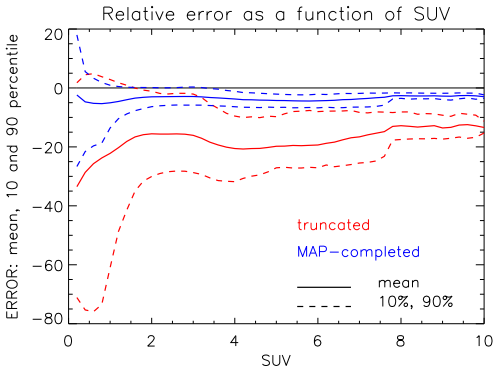

Fig. 2. The relative error in the reconstructed PET image as a function of the reference SUV value. For each SUV value, the mean relative error and the [10%, 90%] confidence interval is shown. In red are the errors for the case with truncation, in blue for the case of truncation + MAP-based completion. The reference PET values are taken from the untruncated attenuation image.

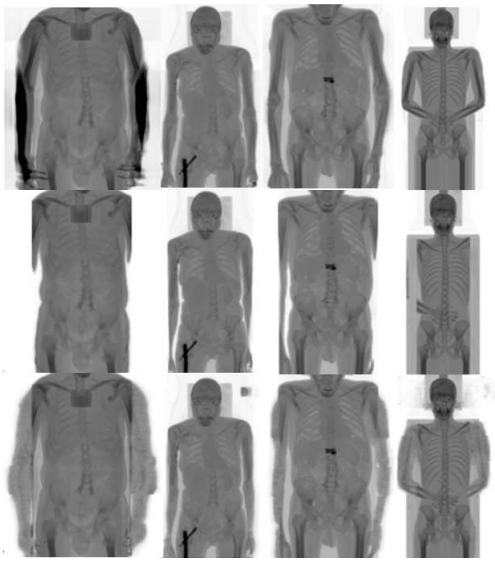

Fig. 3. Maximum intensity projections of the original (top row) and truncated CT-based attenuation map (middle row), and the corresponding images completed with MLAA (last row).

B. Completion of a segmented attenuation map

As mentioned above, converting the MRI-voxel values to linear attenuation coefficients at 511 keV is a non-trivial problem. In particular the identification of bone is problematic. Some currently available segmentation methods produce approximate attenuation maps, where bone and soft tissue are combined in a single tissue class, which is given the attenuation coefficient of soft tissue. To simulate this approach, the CT-attenuation maps were segmented accordingly, and the performance of MLAA for estimating truncated parts was assessed as before. Figure 4 shows the results for the same study as in figure 1. Also for the other studies, the MLAA completions were very similar to that obtained using the non-segmented attenuation maps.

C. Influence of scatter correction

In the experiments presented above, an estimate of the scatter contribution was created with the scatter correction algorithm of [16], using the original, non-truncated attenuation map. In practice, this attenuation map will not be available, and some other, probably less accurate first estimate for the scatter contribution will have to be used. To evaluate the

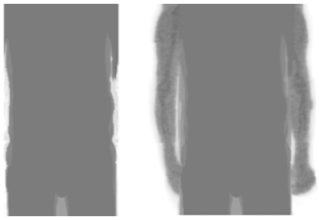

Fig. 4. Maximum intensity projection of the truncated segmented attenuation map (left) and the corresponding image completed with MLAA (right).

sensitivity of the MLAA performance to the scatter estimate, the MLAA algorithm has been applied to the patient studies without scatter correction at all (i.e. s_i in (4) was set to zero). A result is shown in figure 5. In the absence of scatter correction, the shape of the arms estimated by MLAA were similar, but the estimated attenuation coefficients were slightly lower than when scatter was taken into account. This indicates that one can make a first MLAA reconstruction without or with approximate scatter correction. With this first attenuation image an accurate scatter estimate can be computed, which would be used for a final MLAA calculation. Alternatively, the scatter estimation could be included as a part of the iterative MLAA procedure.

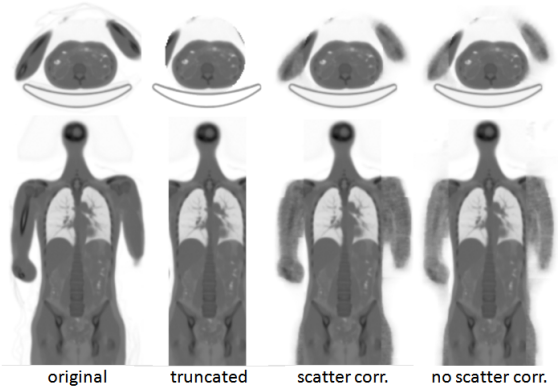

Fig. 5. Transaxial and coronal slices of the original attenuation image, the truncated image, and the MLAA images obtained with and without scatter correction.

D. MLAA-reconstruction of cold objects

The previous experiments indicate that MLAA is capable of producing a useful estimate of arms and shoulders of a patient if these have been truncated in the attenuation image. In these studies, the tracer was ^{18}F-FDG, which has a non-specific accumulation in the entire body. Therefore, these experiments do not predict the performance of MLAA for estimating the attenuation by cold objects that might be in the scanner but are not seen in the (truncated) anatomical image. In particular, in PET-MRI systems, coils may be present in the PET-field of view, and these coils are not seen in the MRI-image.

As a first assessment of MLAA performance for reconstructing the attenuation of such cold objects, a simulation has been carried out. The NCAT phantom [17] was used to create a voxel model of the attenuation and activity images for a PET ^{18}F-FDG study. In front of the patient, 6 rods were placed. Three rods had a diameter of 10 mm and attenuation values of 0.2, 0.15 and 0.095/cm (i.e. higher than or equal to tissue). The other three rods had a diameter of 6 mm and

attenuation coefficients of 0.095, 0.08 and 0.06/cm (i.e. less than or equal to tissue). A fully 3D PET acquisition using the Siemens TruePoint PET system geometry was simulated using analytical projection with attenuation. A noisy-free scatter distribution was added. The resulting maximum count in the noise-free sinogram was 15, Poisson noise was added accordingly. The true and truncated attenuation images are shown in figure 6. The rods are not seen in the truncated attenuation image. Figure 6 also shows the MLAA-completion of the attenuation image. All six rods can be identified in the reconstruction. The reconstruction of the rods is better for the thicker and denser rods.

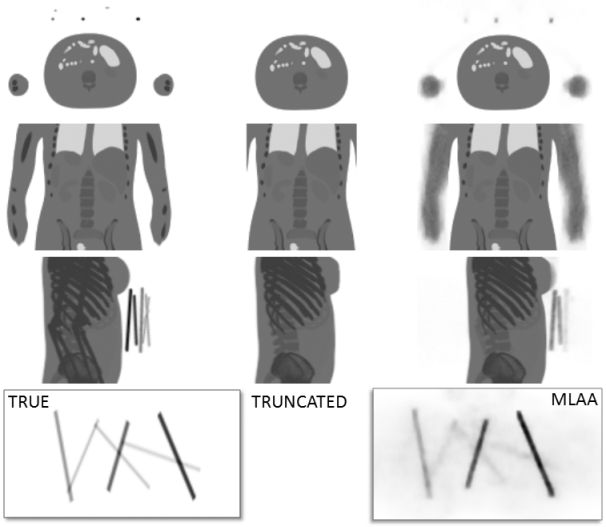

Fig. 6. The left column shows a transaxial slice, a coronal slice and a maximum intensity projection of the true attenuation image; the image at the bottom left is a maximum intensity projection of the six rods located in front of the patient. The central column shows the corresponding images after trucnation. This image does not contain the rods. The right column shows the corresponding images after MLAA-completion.

IV. Discussion

In experiments not shown here, we found that MLAA did not produce good reconstructions of the patient table, but it did reconstruct small metal objects present in the table. We assume that small attenuating objects yield very localized inconsistencies in the sinogram, which are more easily reconstructed that the inconsistencies produced by large smooth objects.

In [5], some artificial operations had to be introduced to ensure that the attenuation of the background was set to zero. Here, this turned out to be unnecessary, because the relative difference prior [13] was used as a regularizer. In a (nearly) zero background, small fluctuations yield large relative differences, and therefore very strong smoothing by the relative difference prior. In contrast, the smoothing effect of the quadratic or Huber priors in the same background would be far less, because the absolute differences between neighboring voxel values are always fairly small in the background.

It has been reported previously that algorithms such as MLAA suffer from "cross-talk" between the activity and attenuation values: a localized decrease of the activity can be compensated well with a corresponding localized decrease of the attenuation, to yield almost the same sinogram. However, in the cold background, MLAA cannot decrease the activity because of the nonnegativity constraint, and as a result, the cross-talk effect does not seem to hamper the reconstruction of detailed cold objects in the background.

V. Conclusion

A modification of the previously developed MLAA algorithm has been proposed, to estimate the missing objects in a truncated attenuation map. The method has been validated on a set of PET/CT patient studies with simulated truncation. The experiments also indicate that the method is not sensitive to small segmentation errors in the known portion of the attenuation map. Failure to correct for scatter resulted in a slight underestimation of the attenuation coefficients, but the shape of the truncated arms was reconstructed well. This suggests that the approach can be combined with image based scatter estimation algorithms. Finally, in a simulation experiment, the MLAA algorithm produced useful reconstructions of cold thin rods with medium to low attenuation coefficients. Therefore, the MLAA method seems to be suitable for the completion of MRI-based attenuation maps in hybrid PET/MRI systems.

References

[1] M Hofmann, B Pichler, B Schölkopf, and T Beyer, "Towards quantitative PET/MRI: a review of MR-based attenuation correction techniques," *Eur J Nucl Med Mol Imaging*, vol. 36 (Suppl 1), pp. 93–104, March 2009.

[2] Y Censor, DE Gustafson, A Lent, and H Tuy, "A new approach to the emission computerized tomography problem: simultaneous calculation of attenuation and activity coefficients," *IEEE Trans Nucl Sci*, vol. NS-26, pp. 2775–2279, 1979.

[3] F Natterer, "Determination of tissue attenuation in emission tomography of optically dense media," *Inverse Problems*, vol. 9, pp. 731–736, 1993.

[4] A Welch, R Clack, F Natterer, and GT Gullberg, "Toward accurate attenuation correction in SPECT without transmission measurements," *IEEE Trans Med Imaging*, vol. 5, pp. 532–541, 1997.

[5] J Nuyts, P Dupont, S Stroobants, R Benninck, L Mortelmans, and P Suetens, "Simultaneous maximum a-posteriori reconstruction of attenuation and activity distributions from emission sinograms," *IEEE Trans Med Imaging*, vol. 18, pp. 393–403, May 1999.

[6] AV Bronnikov, "Reconstruction of attenuation map using discrete consistency conditions," *IEEE Trans Med Imaging*, vol. 19, pp. 451–462, May 2000.

[7] A Krol, JE Bowsher, SH Manglos, DH Feiglin, MP Tornai, and F. Deaver Thomas, "An EM algorithm for estimating SPECT emission and transmission parameters from emission data only," *IEEE Trans Med Imaging*, vol. 20, pp. 218–232, March 2001.

[8] VY Panin, GL Zeng, and GT Gullberg, "A method of attenuation map and emission activity reconstruction from emission data," *IEEE Trans Nucl Sci*, vol. 48, pp. 131–138, 2001.

[9] F Crepaldi and AR De Pierro, "Activity and attenuation reconstruction for positron emission tomography using emission data only via maximum likelihood and iterative data refinement," *IEEE Trans Nucl Sci*, vol. 54, pp. 100–106, 2007.

[10] A Salomon, V Schulz, R Brinks, B Schweizer, A Goedicke, and T Aach, "Iterative generation of attenuation maps in TOF-PET/MR using consistency conditions," *J Nucl Med*, vol. 50 (Suppl 2), pp. 2013, 2009.

[11] A Salomon, V Schulz, B Schweizer, A Goedicke, and Til Aach, "Simultaneous reconstruction of activity and attenuation in multi-modal ToF-PET," *10th International Meeting on Fully Three-Dimensional Image Reconstruction in Radiology and Nuclear Medicine*, pp. 339–342, 2009.

[12] CM Laymon and JE Bowsher, "A log likelihood based method for recovery of localized defects in PET attenuation-correction images," *IEEE Nucl Sci Symp Conf Record*, pp. 2710–2714, October 2004.

[13] J Nuyts, D Bequé, P Dupont, and L Mortelmans, "A concave prior penalizing relative differences for maximum-a-posteriori reconstruction in emission tomography," *IEEE Trans Nucl Sci*, vol. 49, pp. 56–60, 2002.

[14] B De Man, J Nuyts, P. Dupont, G. Marchal, and P. Suetens, "Reduction of metal streak artifacts in x-ray computed tomography using a transmission maximum a posteriori algorithm," *IEEE Trans Nucl Sci*, vol. 47, pp. 977–981, March 2000.

[15] RS Larkin MH Hudson, "Accelerated image reconstruction using ordered subsets of projection data," *IEEE Trans Med Imaging*, vol. 13, pp. 601–609, 1994.

[16] CC Watson, "New, faster, image-based scatter correction for 3d pet," *IEEE Trans Nucl Sci*, vol. 47, pp. 1587–1594, 2000.
[17] WP Segars and BMW Tsui, "Study of the efficacy of respiratory gating in myocardial SPECT using the new 4-D NCAT phantom," *IEEE Trans Nucl Sci*, vol. 49, pp. 3, 675-679 2002.